Princeton Plasma Physics Laboratory

PPPL- 4659

PPPL- 4659

The Relationships Between ELM Suppression, Pedestal Profiles, and Lithium Wall Coatings in NSTX

D.P. Boyle, R. Maingi, P.B. Snyder, J. Manickam, T.H. Osborne, R.E. Bell, B.P. LeBlanc and the NSTX Team

August, 2011

Prepared for the U.S. Department of Energy under Contract DE-AC02-09CH11466.

Princeton Plasma Physics Laboratory
Report Disclaimers

Full Legal Disclaimer

Trademark Disclaimer

PPPL Report Availability

Princeton Plasma Physics Laboratory:

http://www.pppl.gov/techreports.cfm

Office of Scientific and Technical Information (OSTI):

http://www.osti.gov/bridge

Related Links:

U.S. Department of Energy

Office of Scientific and Technical Information

Fusion Links

The relationships between ELM suppression, pedestal profiles, and lithium wall coatings in NSTX

D P Boyle[1], R Maingi[2], P B Snyder[3], J Manickam[1], T H Osborne[3], R E Bell[1], B P LeBlanc[1], and the NSTX team

(email: dboyle@pppl.gov)

[1] *Princeton Plasma Physics Laboratory, Princeton, NJ 08543 USA*

[2] *Oak Ridge National Laboratory, Oak Ridge, TN 37831 USA*

[3] *General Atomics, San Diego, CA 92121 USA*

Abstract. Recently in the National Spherical Torus Experiment (NSTX), increasing lithium wall coatings suppressed edge localized modes (ELMs), gradually but not quite monotonically. This work details profile and stability analysis as ELMs disappeared throughout the lithium scan. While the quantity of lithium deposited between discharges did not uniquely determine the presence of ELMs, profile analysis demonstrated that lithium was correlated to wider density and pressure pedestals with peak gradients farther from the separatrix. Moreover, the ELMy and ELM-free discharges were cleanly separated by their density and pedestal widths and peak gradient locations. Ultimately, ELMs were *only* suppressed when lithium caused the density pedestal to widen and shift inward. These changes in the density gradient were directly reflected in the pressure gradient and calculated bootstrap current. This supports the theory that ELMs in NSTX are caused by peeling and/or ballooning modes, as kink/peeling modes are stabilized when the edge current and pressure gradient shift away from the separatrix. Edge stability analysis using ELITE corroborated this picture, as reconstructed equilibria from ELM-free discharges were generally farther from their kink/peeling stability boundaries than ELMy discharges. We conclude that density profile control provided by lithium is the key first step to ELM suppression in NSTX.

1. Introduction

1.1 Edge localized modes

Edge localized modes (ELMs) are rapidly growing instabilities that commonly occur in the sharp gradient "pedestal" region at the edge of high-confinement (H-mode) tokamak discharges. ELMs are undesirable partly due to the reduction of plasma performance from periodic loss of confinement, but mainly because the rapid ejection of particles leads to extremely large heat fluxes at the divertor which would exceed the limits of proposed materials [1]. For example, ITER will experience unacceptable damage to its plasma facing components unless ELMs can be eliminated or reduced in magnitude by ~95%. As a result, substantial effort has been devoted to the observation and theory of ELMs in order to develop methods to mitigate their potentially crippling effects for large tokamaks [2].

ELMs are typically observed as periodic bursts in D_α (n=3 to n=2 transition) emission in the divertor region of a tokamak [3]. Different types of ELMs are observed with differing fractional losses in stored energy $\Delta W/W$ ranging from up to 20% for giant Type I ELMs [4] to less than 1% for small, "grassy" ELMs [5], e.g., Type V ELMs [6]. The most widely accepted theory explaining the instability is that edge localized modes occur when the plasma edge becomes unstable to current driven peeling or kink modes, and/or pressure driven ballooning modes [7-9]. In this regard, a useful visualization tool is the peeling-ballooning stability diagram. Here, a plasma equilibrium is unstable when its combination of pedestal current and pressure gradient falls outside of a stability boundary, which is determined by shaping and other factors. Although imperfect, this picture has successfully explained the features of the periodic "ELM cycle" and has suggested mechanisms for the different types of ELMs observed in tokamaks [9].

Along with their negative effects, ELMs have the beneficial property of preferentially ejecting impurities from the plasma, especially those with high charge state. Experiments on a range of devices have shown that true ELM-free H-mode is plagued by a secular increase in radiated power due to increased impurity accumulation. As a result, research into methods of suppressing ELMs is now accompanied by research into methods of creating ELMs in a controlled manner for impurity control, e.g.

with pellet injection [10] or with specially tailored magnetic perturbations [11]. ELM pace-making by magnetic perturbations is also the only way to stop the steady rise in line-averaged density that is otherwise observed in nearly all NSTX H-mode discharges [12]. Attractive regimes with suppressed ELMs that do not suffer from impurity accumulation have also been demonstrated, including the quiescent H-mode [13] and use of external resonant magnetic perturbations (RMP) [14]. The QH-mode relies on a steady, saturated edge instability to eject impurities and reduce edge current, while RMP H-mode breaks up magnetic surfaces and also reduces the edge pressure gradient [15]. We differentiate these "quiescent" regimes from "true" ELM-free H-mode which demonstrates different physics, as the edge remains stable and transport is not enhanced.

1.2 Lithium wall coatings and ELMs

Use of lithium wall coatings can result in true ELM-free H-mode, with the associated impurity accumulation. Lithium is one of several materials that have been proposed as a liquid first wall, which would be self healing and could flow to improve power handling. Lithium is unique among candidate liquid metals in that it is chemically reactive with atomic hydrogen and acts as a getter pump. This means that it reduces recycling, which is predicted to have profound effects on the plasma [16,17]. Recycling from a surface is characterized by a recycling coefficient, defined as the ratio of the flux of neutral atoms entering the plasma from the wall to the flux of ions escaping to the wall from the plasma, and is partly measured by D_α emission. Lithium wall conditioning led to improved performance "supershots" in TFTR, with increased confinement, reduced D_α emission, and lower edge density [18]. Similarly, a liquid lithium tray limiter in CDX-U led to greatly improved confinement, reduced D_α emission, and higher edge temperatures [19]. Based on these experimental observations and theory based modeling, lithium is predicted to reduce recycling and lead to wider density gradients and flatter temperature profiles [20].

In the 2005 campaign, lithium was introduced into the National Spherical Torus Experiment [21] (NSTX) with the goal of controlling the ubiquitous rise in plasma density and making the same performance gains seen in other devices. Lithium was initially applied via pellet injection; the Lithium Evaporator (LITER) system has been used since the 2006 campaign [22]. An experiment [23] was

performed in the 2007 campaign to study the effects of lithium on reference H-mode discharges with plasma current I_p=1 MA, neutral beam heating power P_{NBI}=4 MW, vacuum on-axis toroidal field B_T=0.45 T, and ordinary Type I ELMs. Using a single, continuously operating lithium evaporator, large lithium coatings (~1 g between discharges) significantly reduced the occurrence of ELMs and caused extended ELM-free periods. Other improvements included decreases in plasma density and inductive flux consumption, and increases in electron temperature, ion temperature, and energy confinement. However, questions remained about the nature and duration of the lithium coatings and the mechanism for ELM suppression.

In order to answer these questions, a subsequent experiment [24,25] was performed to investigate phenomenology of ELM suppression caused by gradually increasing lithium wall conditioning. In previous work [26], we compared the profiles and stability of the endpoints of the experiment, i.e., ELMy pre-lithium discharges versus completely ELM-free discharges with thick lithium coatings. The conclusions were that lithium widened the density pedestal and shifted it away from the separatrix, causing similar changes in the edge pressure and current profiles, and that this caused the plasma to be farther from its peeling-ballooning stability boundary, i.e., more stable. Edge transport analysis of this sequence of discharges was also recently documented [27].

In the remainder of this paper, we first recap the experimental procedure and the previously described results of increasing lithium on discharge evolution and ELM behavior. We extend the work beyond [25,26], with profile analysis for the *entire* scan, and the results of the stability analysis for selected discharges, documenting the evolution with increasingly thick lithium coatings. Finally, we summarize this new analysis, which shows that ELMs disappeared gradually but non-monotonically with increasing wall coatings, and that the density and pressure profile characteristics organize the ELMy and ELM-free data.

2. Experiment

This experiment consisted of NSTX discharges 129015 – 129041, the first discharges of the 2008 campaign to use lithium. Elements of this discharge sequence have been previously described [24-28],

and so a brief summary is given here. The discharges were based on a scenario observed in an Alcator C-Mod/MAST/NSTX similarity experiment [29] that reliably produced ordinary Type I ELMs of magnitude $\Delta W/W \sim$ 2-5% and nominal frequency ~100 Hz. These discharges used I_p = 0.8 MA, B_T = 0.45 T, and P_{NBI} = 4 MW, and the ion $B\times\nabla B$ drift was toward the lower divertor. The boundary shape was a near double-null diverted configuration with elongation $\kappa \sim$ 1.8-1.9, upper triangularity $\delta_u \sim 0.53$, lower triangularity $\delta_l \sim 0.46$, and $\delta_r^{sep} \sim$ -5 mm. δ_r^{sep} is defined as the distance between the two X-points (mapped to the outer midplane), with the convention that the lower X-point is closer to the plasma for $\delta_r^{sep} < 0$.This was the first experiment to use the upgraded dual evaporator LITER lithium deposition system [24,30,31]. Its shutters were closed during the 0.6-1 s high-power discharges and the ~6.5 min He glow conditioning that followed each discharge. The shutters were then opened for ~10 minutes, until the subsequent discharge. This procedure avoided co-deposition of helium, and allowed for lithium deposition that was concentrated in the lower divertor while still providing good toroidal coverage. Specifically, the poloidal deposition profile was a Gaussian centered at major radius R ~ 30 cm with half width ~ 60 cm [23,31]. Recycling occurs mainly at the outer strike point; at R ~ 80 cm lithium thickness was ~ 70% of the central value. Toroidal deposition was approximately even in two sections with line of sight to both evaporators, covering ~ 70% of the lower divertor. In the remaining 30% of the lower divertor that was shadowed from one of the evaporators by the center stack, deposition was also even but at ~40% of the thickness of the high deposition region. The toroidally averaged thickness at the outer strike point was ~ 0.5 nm per mg of evaporated lithium; the minimum thickness was about half that.

For each discharge in the experiment, the quantity of lithium deposited is shown in Figure 1. Both the fresh lithium deposited since the previous discharge (left axis, black Δ) and the cumulative lithium deposited since the start of the experiment (right axis, blue □) are important, as the wall coatings are partially passivated during each discharge. All previously introduced lithium had been removed from the machine during the previous vacuum break, so discharges 129015 – 129020 served as a true no lithium baseline. Lithium evaporation began with 110 mg (55 nm thickness) applied before discharge 129021 and ~150 mg (75 nm) applied before each of the next 8 discharges. Deposition was increased to 260 mg (130

nm) before discharge 129030 and was further increased over the subsequent discharges, increasing to 930 mg (465 nm) of fresh lithium before discharge 129041. For convenience, we will define between-discharge coatings < 400 mg (200 nm) as "intermediate" and > 400 mg as "thick". Cumulatively, 7.8 g (3.9 μm) of lithium was introduced by the end of the experiment.

3. Discharge and ELM evolution during the lithium coating scan

The effect of increasing lithium wall coatings on discharge evolution is shown in Figure 2 for three discharges (black: pre-lithium; orange: intermediate lithium coating; blue: thick lithium coating, reduced power). Increasing lithium coatings resulted in longer discharges [Fig. 2(a)], as well as slower density growth [Fig. 2(c)], though the same density was eventually achieved. Note that the intermediate discharge experienced a locked mode at 0.57 s. Neutral beam heating was incrementally reduced for subsequent discharges, which suffered the same instability, until a sustained discharge was achieved with increased gas fueling and 2 MW of injected power [Fig. 2(b)]. Despite the reduction in heating power, plasma stored energy was unchanged, reflecting an approximately 50% increase in energy confinement time relative to the reference ELMy discharge [Fig. 2(d-e)]. This improvement in performance occurred even though greater accumulation of impurities caused radiated power to continue to increase throughout the discharge [Fig. 2(f)]. A major reason for these performance improvements (and the impurity accumulation) was the suppression of ELMs. ELMs were significantly reduced by intermediate lithium coatings and completely eliminated by large quantities of lithium [Fig. 2(g-i)]. Recycling, as indicated by baseline D_α emission, was also reduced by the increasing lithium coatings. Once a sustained, ELM-free discharge was achieved, the beam power was again increased. With 3 MW of beam heating, the final discharge reached the global stability limit before reaching the edge/ELM stability limit [25,26].

Examination of the lower divertor D_α emission measurements [Fig. 3a] reveals key facets of how the ELM behavior progressed throughout the discharge sequence. The first few with-Li discharges (129021-129023) lasted longer and had somewhat reduced ELM frequencies, but ELMs continued for the duration of those discharges. As more lithium was added, recycling dropped and discharges (129025, 129030-129031) with short ELM-free periods began to emerge. However, the process was not monotonic

at these intermediate lithium deposition levels. Even as more lithium was added, fully ELMy discharges returned (129027, 129029, 129032). These ELMy discharges all coincided with a sustained period of low confinement, high recycling L-mode at the end of the previous discharge (129026 had no neutral beam heating; 129028 and 129031 suffered locked modes). Discharges 129029 and 129030 also suffered locked modes and ended in periods of L-mode but were followed by discharges with ELM-free phases. However, these L-mode periods were shorter and had very low stored energy. One possible explanation for the return of ELMs is that the accumulated lithium was passivated by the sustained L-mode discharges, and the amount of fresh lithium in these discharges was by itself insufficient to suppress ELMs. Discharges 129033, 129036, 129038 and 129041 were ELM free despite following periods of sustained and/or high stored energy L-mode. In these cases, the thick coatings of fresh lithium were able to suppress ELMs by themselves, regardless of the condition of the previously accumulated lithium.

In order to quantify the changes in ELM behavior, the average frequency of ELMs during one or more ~100-200 ms time intervals was computed for each discharge in the experiment. These intervals were selected based on approximately constant ELM frequency during the fully evolved H-mode portion of the discharge ($t > 0.3$ s) and before any major loss of confinement. Fig. 3(b) plots the ELM frequency of these intervals versus NSTX discharge number. In order to visually separate time intervals within the same discharge, a small, arbitrary fraction was added to the discharge number for intervals occurring later in the discharge. Where the time interval was also successfully used for a profile fit (see section 4.1), it is shown in black. Intervals without a profile fit are shown in light blue; discharges which failed to achieve a sustained H-mode are shown below the x-axis as red Xs. Though ELMs were steady for the first few discharges and absent in the final discharges, the intermediate region did not show a monotonic dependence.

Figures 3(c-d) plot ELM frequency versus lithium deposited since the previous discharge and cumulative lithium deposited. Both measures also show non-monotonic relationships between ELM frequency and quantity of lithium. Increasing lithium was clearly correlated to suppression of ELMs, though ELM behavior was not solely determined by the quantity of lithium deposited at the intermediate

amounts used for the majority of this experiment. While very interesting, in practice these intermediate deposition levels are rarely used during normal lithium operations. Both here and in other experiments [30], "thick" lithium coatings with two LITERs consistently resulted in ELM-free discharges, given proper fueling, heating, and divertor configuration. Still, we are motivated to understand the details behind the return of ELMs after continued lithium deposition, though it is beyond the scope of this paper. A related goal is to identify the optimal amount of deposition in order to reduce the risk of long term surface buildup and flaking, which can cause operational problems. Other important issues are raised by recent work, which asks (1) why the coatings need to be so thick to be effective and (2) why plasma performance continues to improve well beyond the minimum thickness, even in the ELM-free regime [32].

4. Profile analysis

4.1 Profile measurement and fitting

In order to investigate how the plasma changed during the experiment, and to compute accurate equilibria for stability analysis, plasma profiles were measured and composite profiles were reconstructed. Electron density, temperature, and pressure profiles were measured with the NSTX multi-point Thomson scattering (TS) system [33], while ion profiles were measured by the charge exchange recombination spectroscopy (CHERS) system [34]. In this experiment, one TS laser was operated at repetition rate 30 Hz. Measurements were made at 30 radial locations on the horizontal midplane, and resolution ranged from ~5-11 cm on the high field side and from ~1-3 cm on the low field side, with the finest resolution near the outboard edge. Relative uncertainty was typically ~2-10% in electron density and temperature, with higher values at the edge. The CHERS diagnostic measured ion temperature, carbon density, and velocity profiles with an integration time of 10 ms and radial resolution ranging from 0.6–3 cm (edge to core). Relative uncertainty was typically ~2-5% in ion density and temperature.

As the profile measurements occurred at fixed locations in real space, small fluctuations in the boundary caused the measurement locations to vary in magnetic flux coordinates. This effect was used with a standard set of procedures and tools [15] to achieve greater resolution than available from a single

profile alone. This "correlated sampling" technique combined 3-6 measurements taken from the inter-ELM periods of ~100-200 ms time intervals, chosen such that total stored energy, line integrated density, and ELM behavior did not vary substantially over the interval. For each TS profile measurement in the interval, an EFIT equilibrium reconstruction [35,36] was calculated and the TS and CHERS profiles were mapped from real space coordinates into normalized poloidal flux coordinates $\psi_N = (\psi - \psi_{core})/(\psi_{separatrix} - \psi_{core})$. All of the data were superimposed, and fit to smoothing splines and modified hyperbolic tangent (mtanh) functions [37]. Note that well resolved profiles could not be fit for every discharge or for every period of unique ELM behavior within each discharge, and mtanh functions usually could only be fit to the electron profiles.

Fits to mtanh functions are useful for comparison as the H-mode pedestal can be captured with five fitting parameters, all of which have direct physical meanings. The entire functional form used in the fitting procedure is given by by $Y(X) = Y_{offset} + (Y_{pedestal} - Y_{offset})\ (½ + ½\ \mathrm{mtanh}(\alpha_{slope}\ , 2(X_{symmetry} - X) / \Delta_{width})$, while the mtanh function itself takes the form $\mathrm{mtanh}(\alpha_{slope}\ , z) = \tanh z + \alpha_{slope} z(½ + ½ \tanh z)$. [37], More compactly, $Y(X) = Y_{offset} + (Y_{pedestal} - Y_{offset})\ (1 + ½\alpha_{slope} z) / (1 + e^{-2z})$, with $z = 2(X_{symmetry} - X) / \Delta_{width}$. An example is plotted in Fig. 4. α_{slope} is the normalized slope inboard of the pedestal, with $\alpha_{slope} > 0$ indicating a monotonic profile and $\alpha_{slope} < 0$ indicating a hollow profile. Y_{offset} is related to the height at the edge, though in practice this term is small and the height at the edge is dominated by the other term. $Y_{pedestal}$ is related to the height of the pedestal, though it is an underestimate for monotonic profiles and can be an overestimate for hollow profiles. The location of the peak gradient is important for MHD stability to peeling and ballooning modes, and is given by $X_{symmetry}$ for $\alpha_{slope} = 0$, though non-zero α_{slope} causes the peak gradient to shift slightly. $X_{symmetry}$ can also be considered the location of the pedestal, and the location of the edge transport barrier that causes the pedestal [38]. Similarly, the mtanh full width Δ_{width} can be considered the width of both the pedestal and the edge transport barrier. Note that both the full- and half-width are used in the literature; we use the full width here.

4.2 Profile results and analysis

Figure 5 compares profile data and fits from four representative discharges: a pre-lithium ELMy discharge (black X), an intermediate lithium deposition discharge with reduced ELM activity (turquoise ◊), an intermediate lithium deposition discharge where ELMs have returned (orange +), and a high lithium deposition ELM-free discharge (blue Δ). Fig. 5(a) shows that intermediate amounts of lithium did not change the electron density profile for $\psi_N > 0.95$, though the reduced ELM discharge had a wider and taller n_e pedestal. The density profile for the intermediate lithium ELMy discharge was similar to the pre-lithium ELMy discharge [Fig. 5(b)]. With larger amounts of lithium, the density pedestal became even wider, shifted away from the separatrix, and was no longer significantly taller than in the ELMy discharges. The electron temperature profiles were all very similar for $\psi_N > 0.95$ [Figs 5(c-d)]. However, average T_e increased with increasing lithium because $|\nabla T_e|$ increased for $\psi_N < 0.95$; this effect was larger in the ELM-free discharges. As the product of the density and temperature, the electron pressure profiles [Fig. 5(e-f)] followed the same trends. The p_e profile outside of $\psi_N = 0.95$ was unaffected by intermediate amounts of lithium, while large quantities caused the p_e pedestal to shift away from the separatrix. The suppression of ELMs coincided with wider and taller p_e pedestals, while the p_e profile for the intermediate lithium ELMy discharge was similar to the pre-lithium ELMy discharge. While the ELM-free ion pressure profiles showed an increase in pedestal width similar to the p_e profile, the changes were much less pronounced [Fig. 5(g-h)]. Thus, the differences in the total pressure profiles [Fig. 5(i)] were mainly due to differences in the p_e profiles. Fig. 5(j) shows that stability to ELMs was not achieved merely by reducing the peak pressure gradient, as 129019 and 129031 have similar peak pressure gradients. Rather, the peak pressure gradients in the ELM-free discharges were wider and farther from the separatrix.

The trends from *all* of the converged profile fits are shown in Fig. 6, which uses the mtanh fit parameters to quantify the changes in the electron profiles with increasing lithium deposition. Profile parameters from ELMy periods (black *) and ELM-free periods (blue ◊) are plotted against the quantity of lithium deposited since the previous discharge. The ELM-free plasmas *consistently* had wide electron density pedestals that grew wider with additional lithium [Fig. 6(a)], with the symmetry point simultaneously shifting away from the separatrix [Fig. 6(b)]. In contrast, the n_e pedestals of ELMy

plasmas were *all* narrower and closer to the separatrix, and neither parameter showed a relationship to the quantity of lithium. This suggests the importance of the density profile to edge stability. Fig. 6(c) shows that the peak magnitude of $|\nabla n_e|$ generally decreased with increasing lithium, though it was not clearly related to ELM behavior. Fig. 6(d) shows that the ELM-free electron temperature pedestals were mostly wider than the ELMy ones. However, a different analysis technique (which otherwise replicated the mtanh results) indicated that this was actually just an artifact of the mtanh fitting function. With a smoothing spline fit to T_e, the ELMy and ELM-free $|\nabla T_e|$ full widths at half maximum fully overlap. In fact, none of the T_e profile parameters showed much relationship to ELM behavior The T_e symmetry point varied relatively little over the entire experiment, also showing no relationship to lithium deposition [Fig. 6(e)]. The peak electron temperature gradient increased with lithium, though it increased with a larger slope in ELMy plasmas [Fig. 6(f)]. In Figures 6(g-h), the electron pressure pedestal full widths and symmetry points tracked each other and their n_e counterparts. p_e and n_e showed the same correlation to lithium and the same clean separation between ELMy and ELM-free discharges. As pressure is an important quantity for MHD stability, this is strong evidence that changes in the profiles led to changes in stability. While ELMy and ELM-free plasmas showed opposite correlations between lithium and the magnitude of the peak electron pressure gradient [Fig. 6(i)], peak $|\nabla p_e|$ itself showed no direct relationship to ELM behavior. As further evidence that the changes in the total pressure were caused mainly by the electrons, plots for the total pressure [Fig. 6(j-l)] were quite similar to the electron pressure plots.

In Figure 7, the fit parameters from ELMy profiles (black *) and ELM-free profiles (blue ◊) are plotted against the ELM frequency of the interval during which they were measured. These plots make clearer which parameters separate the ELMy and ELM-free profiles and which do not. The density pedestal widths and symmetry points are seen in Figures 7(a-b) to be good ordering parameters. Furthermore, the intermediate n_e widths and symmetry points occurred during the ELM-free periods of otherwise ELMy discharges, suggesting a *continuous* relationship between these parameters and robustness to ELMs. In Figure 7(c), the peak $|\nabla n_e|$ did not separate the ELMy plasmas from the ELM-free. Figures 7(d-f) show that none of the T_e parameters determined ELM stability, while in Figures 7(g-i) the

electron pressure shows the same trends as the density. As in Figure 6, the total pressure closely tracked the electron pressure; therefore it is not shown in Figure 7.

In general, the edge profile parameters of ELMy plasmas were all fairly similar, or at least showed no relationship to whether the discharge occurred before or after the introduction of lithium. The similarity of the edge profiles gives some additional support to the explanation that the lithium had been passivated by the period of L-mode in the previous discharge. Of course, it may just be beyond our ability to reconstruct subtle differences due to, for example, a smoothing effect introduced by the conditional averaging procedure.

In contrast, the differences in the ELM-free plasmas intensified with greater lithium deposition. While lithium affected both the ELM behavior and edge profiles, the quantity of lithium deposited did not uniquely determine either. However, the density and pressure pedestal widths and symmetry points consistently partitioned the ELMy and ELM-free discharges. In other words, lithium *only* suppressed ELMs when it also modified the density profile. This observation implies a straightforward mechanism for the suppression of ELMs with lithium wall coatings. By reducing recycling and changing edge transport [27], lithium shifted the peak density gradient inward away from the separatrix. The bootstrap current and pressure gradient peaks followed, reducing the drive for the kink/peeling part of the underlying instabilities.

5. Stability analysis

To perform the stability analysis, free boundary equilibria were calculated using EFIT constrained by the fit pressure profiles, and by current profiles calculated using the Sauter neoclassical formula for the bootstrap current [39]. While the lack of an edge current measurement is a major source of uncertainty in the stability analysis, we note that the neoclassical value was found to be in agreement with lithium-beam measurements on DIII-D [40]. In order to map out the stability boundary, additional fixed boundary model equilibria were calculated with variations in the edge current and pressure gradient, as in [15].

The stability of the equilibria was calculated using the ELITE code [41,42]. The stability criterion is given by $\gamma_0/(½\ \omega_{*i})$, where γ_0 is the linear growth rate of the peeling-ballooning mode and ω_{*i} is the diamagnetic drift frequency. Contour plots of $\gamma_0/(½\ \omega_{*i})$ versus normalized edge current and normalized pressure gradient are shown in Figure 8 for four discharges selected for especially sharp transitions in ELM behavior. The crosshairs are centered on the experimental equilibrium and represent relative error in normalized edge current and normalized pressure gradient of 30% and 20%, respectively. The red region was unstable with $\gamma_0/(½\ \omega_{*i}) > 0.15$; the blue region was stable with $\gamma_0/(½\ \omega_{*i}) < 0.05$. We note that $\gamma_0/(½\ \omega_{*i}) = 1$ marked the stability boundary to intermediate-*n* peeling-ballooning modes in DIII-D [15], but the stability criterion has been found to be an order of magnitude lower for low-*n* kink/peeling modes in NSTX [26,43]. In all of the discharges in this experiment, the equilibrium was closer to the current driven kink/peeling stability boundary, with the pressure driven ballooning boundary well off to the right hand side of the axis. In Fig. 8(a), a pre-lithium ELMy discharge was very close to the stability boundary. In Fig. 8(b) the stability boundary was much farther away for a discharge in which ELMs had been suppressed by intermediate lithium coatings. The improved stability was partly due to reduction of the edge current. More importantly, the stability boundary shifted to the left and upward; even with edge current comparable to the value in panel (a), this discharge would have been more stable. This shift in stability was probably because the pressure gradient and current peaks were shifted inward away from the separatrix. Fig. 8(c) shows a discharge in which ELMs returned, despite continued lithium deposition. Here, the stability boundary was very similar to the pre-lithium case, though the discharge had a significantly larger edge current and pressure gradient. In the thick lithium coating, ELM-free discharge, [Fig. 8(d)], the edge current was about the same as the other ELM-free case, but the pressure gradient was lower, which in and of itself is destabilizing for kink/peeling modes. However, the stability boundary shifted to the left and up as the pressure gradient and current peaks shifted inward, making this discharge robustly stable. To summarize: the ELM-free equilibria in Fig. 8 were farther from their stability boundaries than the ELMy discharges. In the ELM-free discharges, the stability boundaries shifted to the left and up as the edge pressure gradient and current peaks widened and shifted away from the separatrix.

The above trend is clear at the endpoints: other no-lithium discharges in this experiment were similar to Fig. 8(a), and thick lithium discharges from other NSTX experiments were similar to Fig. 8(d). Other intermediate lithium discharges in this experiment were more similar to Fig. 8(b) than Fig. 8(c). That is, their edge currents were ~20-40% below the stability boundary, whether or not they were ELMy. Given the number of steps involved in calculating the stability, it is unsurprising that it is difficult to resolve the precise transition from ELMy to ELM-free. However, it is clear that in general, ELM-free equilibria were farther from their stability boundaries than the ELMy discharges.

6. Summary and conclusions

In this experiment, increasing lithium wall coatings in NSTX resulted in gradual but not quite monotonic suppression of ELMs. With intermediate lithium wall coatings, increasingly long ELM-free periods emerged; with thicker coatings completely ELM-free discharges were achieved. However, completely ELMy discharges returned throughout the experiment, even with continued lithium coatings. We speculate that L-mode periods in the preceding discharge passivated the accumulated lithium. Despite increased radiated power, the suppression of ELMs led to large gains in confinement and overall plasma performance. With thick lithium coatings, the plasma reached a global stability limit while the edge remained stable to ELMs.

Profile analysis demonstrated that lithium had a greater effect on the electrons than the ions. Furthermore, it modified the edge density profile much more than the edge temperature. The n_e pedestals became wider and shifted inward with increasing lithium, while T_e increased farther in, i.e. $\psi_N < 0.95$. The pressure profiles reflected the changes in the n_e and T_e profiles, as the p_e pedestals became taller, wider, and shifted away from the separatrix. However, these effects were only observed in discharges where lithium had suppressed ELMs; the ELMy discharges showed little or no relationship between the pedestal parameters and the quantity of lithium deposited. This implies that ELM suppression is closely related to n_e and p_e profile modification. Indeed, the ELMy and ELM-free discharges were consistently discriminated by their density and pressure pedestal widths and symmetry points. Furthermore, the data suggest a continuous relationship between the pedestal parameters and stability to ELMs. The discharges

with both ELMy and ELM-free phases had intermediate pedestal widths and symmetry points, while the pedestal of the completely ELM-free discharge was widest and farthest from the separatrix. All of these observations support the theory that ELMs in NSTX are caused by kink/peeling modes, which are stabilized as the edge current and pressure gradient shifts away from the separatrix.

Further support comes from edge stability analysis using the ELITE code. Reconstructed equilibria from ELM-free discharges were far from their stability boundaries, while with a few exceptions, ELMy discharges were closer to the kink/peeling instability. The conclusion from this is that stabilization of kink/peeling modes due to modification of the density profile is a key part of the mechanism by which increasing lithium wall coatings gradually suppressed ELMs in NSTX.

Acknowledgements

This research was supported in part by the U.S. Deptartment of Energy under contracts DE- AC05-00OR22725, DE-AC02-09CH11466, and DE-FC02-04ER54698. We gratefully acknowledge the contribution of the NSTX technical and operations staff. D. Boyle was supported by a DOE Fusion Energy Sciences fellowship.

Figure Captions

Figure 1: Lithium deposited vs. NSTX discharge number. After a 6 discharge no-lithium baseline, ~fixed lithium deposition before each of the next 9 discharges, followed by increasing deposition before the last 11. Deposition began before discharge 129021. Fresh lithium deposited since previous discharge is plotted against left axis (black Δ); cumulative lithium is plotted against right axis (blue □).

Figure 2: Lithium coatings improved performance and suppressed ELMs. Discharge evolution comparisons of: (a) plasma current I_p, (b) neutral beam injected power P_{NBI}, (c) line-averaged density from Thomson Scattering n_e, (d) stored energy from equilibrium reconstruction W_{MHD}, (e) energy confinement time relative to ITER97L scaling, (f) total radiated power P_{rad}, and (g-i) divertor D_α emission. Measurements were from a pre-lithium ELMy discharge (black), an intermediate lithium discharge with reduced ELM activity (orange), and a thick lithium coating, ELM-free discharge with reduced NBI power (blue).

Figure 3: ELMs gradually yet fitfully disappeared with increasing lithium wall coatings. (a) ELM activity is shown by divertor D_α emission for selected NSTX discharges. Other discharges are omitted due to redundancy (129016-129019, 129023), failed discharge (129026, 129034), or early termination due to locked modes (129028, 129033, 129035-129037). (b) ELM frequency vs. NSTX discharge number. ELM frequencies are averaged over time intervals with consistent ELM behavior; when possible these were the same time intervals used for profile fitting (black ◊). Intervals in which a profile could not be fit are shown in blue; discharges which failed to achieve H-mode are shown as red Xs below the axis; no actual ELM frequency is implied. In order to visually separate time intervals within the same discharge, a small, arbitrary fraction was added to the discharge number for intervals occurring later in the discharge. (c) ELM frequency vs. lithium deposited since previous discharge, (d) ELM frequency vs. cumulative lithium deposited

Figure 4: The mtanh fit captures the important elements of the H-mode pedestal with 5 intuitive parameters. An example electron temperature profile is shown. α_{slope} is the normalized slope inboard of the pedestal, with $\alpha_{slope} > 0$ indicating a monotonic profile and $\alpha_{slope} < 0$ indicating a hollow profile. T_e^{offset} is related to the temperature in the scrape-off layer, and $T_e^{pedestal}$ is approximately the temperature at the top of the pedestal. $\psi_{symmetry}$ and Δ_{width} are respectively the location and full width of the pedestal, or alternatively, the edge transport barrier.

Figure 5: Lithium wall coatings drastically modified edge profiles. Edge profile comparisons of (a, b) electron density n_e, (c, d) electron temperature T_e, (e, f) electron pressure p_e, (g, h) ion pressure p_i, (i) total pressure p_{e+I}, and (j) pressure gradient $dp/d\psi_N$. Profiles are from a pre-lithium ELMy discharge (black X), an intermediate lithium discharge with reduced ELM activity (turquoise ◊), an intermediate lithium discharge where ELMs have returned (orange +), and a high lithium deposition, ELM-free discharge (blue Δ). Fits are obtained from multiple time slices mapped to the nearest equilibrium. The x-axis is normalized poloidal flux: $\psi_N = (\psi - \psi_{core})/(\psi_{separatrix} - \psi_{core})$, where ψ_{core} and $\psi_{separatrix}$ are the poloidal flux values at the magnetic axis and separatrix, respectively.

Figure 6: Density and pressure pedestals became wider and farther from separatrix with increasing lithium wall coatings while temperature showed no relationship to lithium. Lithium deposited since previous disharge is plotted vs. for ELMy (black *) and ELM free plasmas (blue ◊): (a) n_e mtanh full width, (b) n_e mtanh symmetry point, (c) peak n_e gradient, (d) T_e mtanh full width, (e) T_e mtanh symmetry point, (f)

peak T_e gradient, (g) p_e mtanh full width, (h) p_e mtanh symmetry point, (i) peak p_e gradient, (j) p_{tot} full width at half maximum, (k) p_{tot} peak gradient location, and (i) peak p_{tot} gradient. Note that the vertical axes have suppressed zeros, and that the p_{tot} profile fit parameters are based on spline fits rather than mtanh fits.

Figure 7: ELM free plasmas had wider density and pressure pedestals that are farther from the separatrix while pedestal gradients and temperature profiles showed no relationship to ELMs. ELM frequency is plotted vs. profile fit parameters for ELMy (black *) and ELM free plasmas (blue ◊): (a) n_e mtanh full width, (b) n_e mtanh symmetry point, (c) peak n_e gradient, (d) T_e mtanh full width, (e) T_e mtanh symmetry point, (f) peak T_e gradient, (g) p_e mtanh full width, (h) p_e mtanh symmetry point, and (i) peak p_e gradient. Note that the horizontal axes have suppressed zeros.

Figure 8: ELM-free plasmas were farther from the kink/peeling stability boundary as calculated by ELITE. Contour plots of the stability criterion, $\gamma_0/(½\ \omega_{*i})$ versus normalized edge current and normalized pressure gradient are shown for four representative discharges. The crosshairs are centered on the experimental equilibrium and represent relative error in normalized edge current and normalized pressure gradient of 30% and 20%, respectively. In the red region, $\gamma_0/(½\ \omega_{*i}) > 0.15$; in the blue region, $\gamma_0/(½\ \omega_{*i}) < 0.05$. Equilibria are from (a) a pre-lithium ELMy discharge, (b) an intermediate lithium discharge with reduced ELM activity , (c) an intermediate lithium discharge where ELMs have returned (no converged kinetic fits in blank space), and (d) a high lithium deposition, ELM-free discharge. Note that the axes have suppressed zeros.

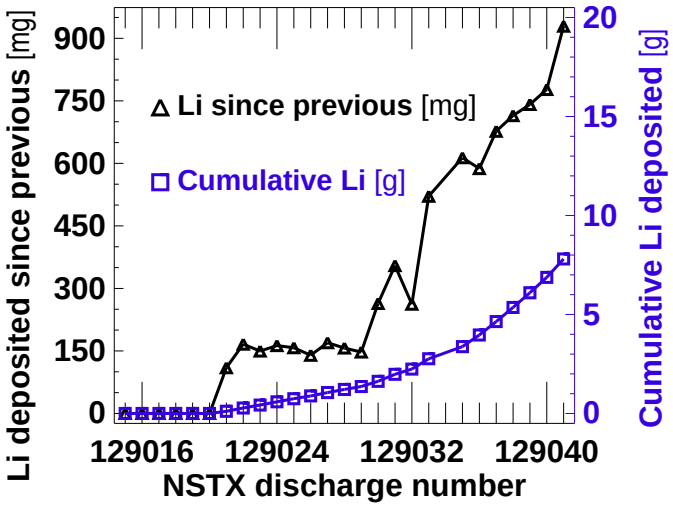

Figure 1: Lithium deposited vs. NSTX discharge number. After a 6 discharge no-lithium baseline, ~fixed lithium deposition before each of the next 9 discharges, followed by increasing deposition before the last 11. Deposition began before discharge 129021. Fresh lithium deposited since previous discharge is plotted against left axis (black Δ); cumulative lithium is plotted against right axis (blue □).

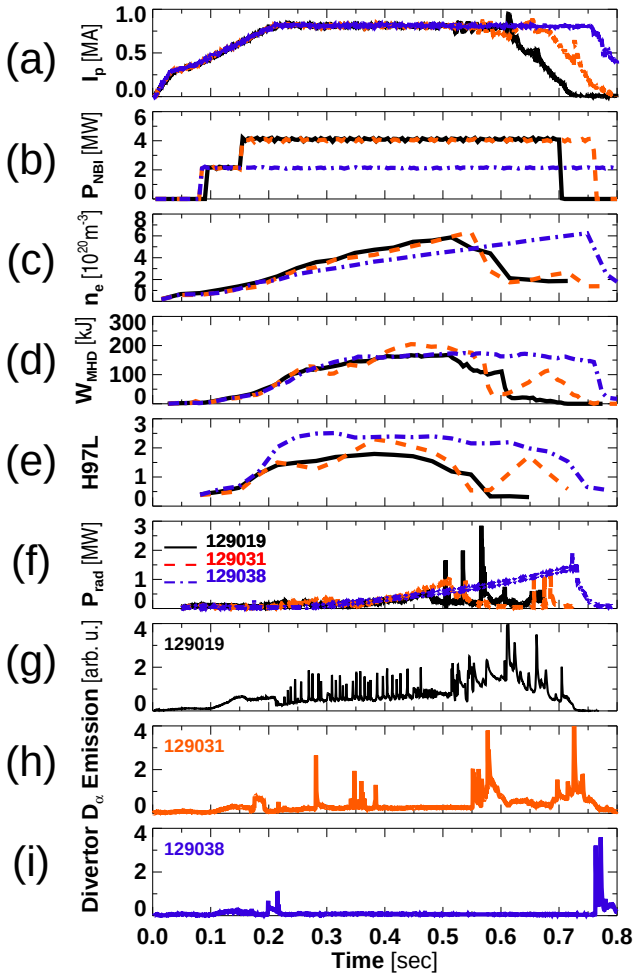

Figure 2: Lithium coatings improved performance and suppressed ELMs. Discharge evolution comparisons of: (a) plasma current I_p, (b) neutral beam injected power P_{NBI}, (c) line-averaged density from Thomson Scattering n_e, (d) stored energy from equilibrium reconstruction W_{MHD}, (e) energy confinement time relative to ITER97L scaling, (f) total radiated power P_{rad}, and (g-i) divertor D_α emission. Measurements were from a pre-lithium ELMy discharge (black), an intermediate lithium discharge with reduced ELM activity (orange), and a thick lithium coating, ELM-free discharge with reduced NBI power (blue).

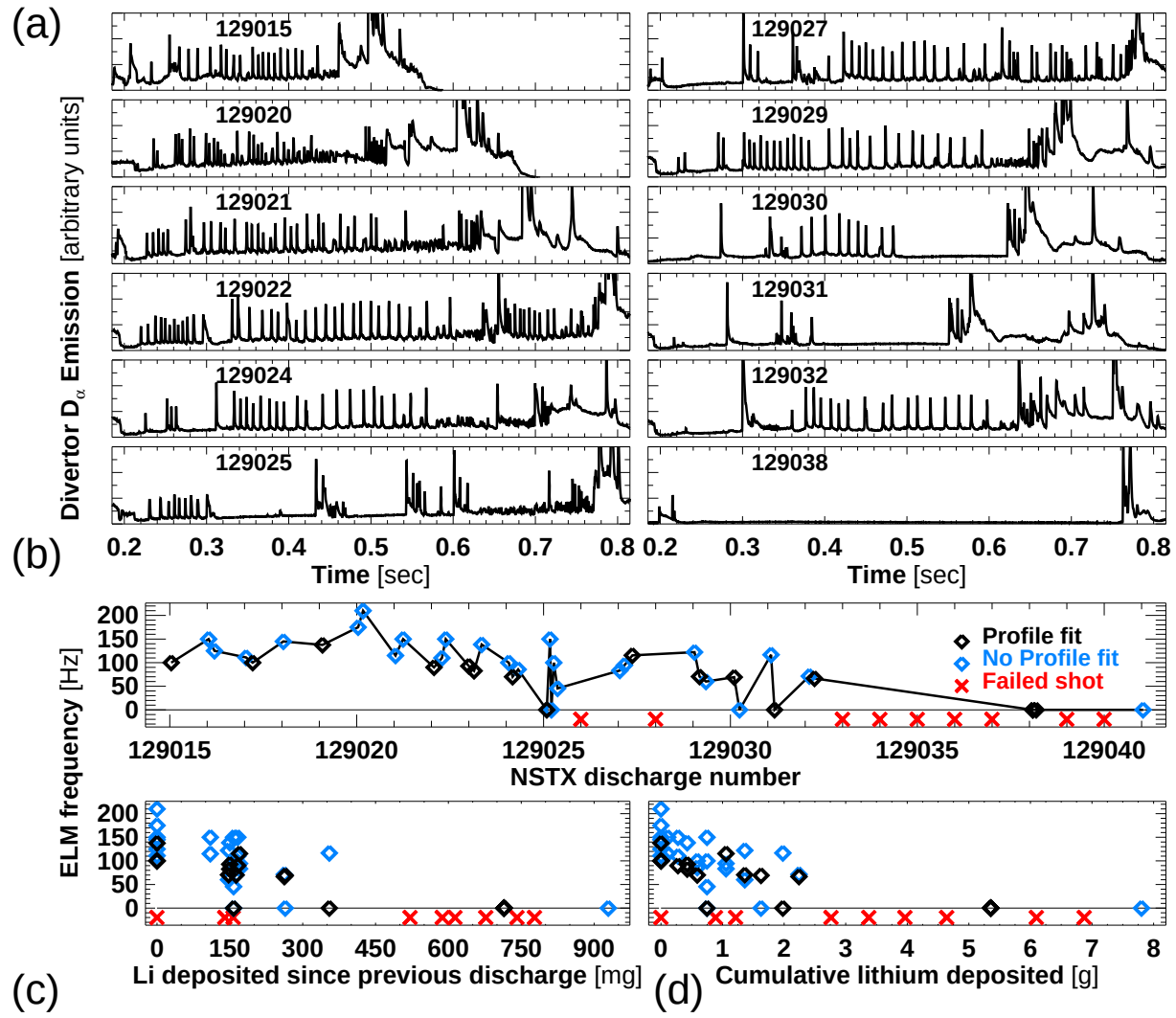

Figure 3: ELMs gradually yet fitfully disappeared with increasing lithium wall coatings. (a) ELM activity is shown by divertor D_α emission for selected NSTX discharges. Other discharges are omitted due to redundancy (129016-129019, 129023), failed discharge (129026, 129034), or early termination due to locked modes (129028, 129033, 129035-129037). (b) ELM frequency vs. NSTX discharge number. ELM frequencies are averaged over time intervals with consistent ELM behavior; when possible these were the same time intervals used for profile fitting (black ◊). Intervals in which a profile could not be fit are shown in blue; discharges which failed to achieve H-mode are shown as red Xs below the axis; no actual ELM frequency is implied. In order to visually separate time intervals within the same discharge, a small, arbitrary fraction was added to the discharge number for intervals occurring later in the discharge. (c) ELM frequency vs. lithium deposited since previous discharge, (d) ELM frequency vs. cumulative lithium deposited

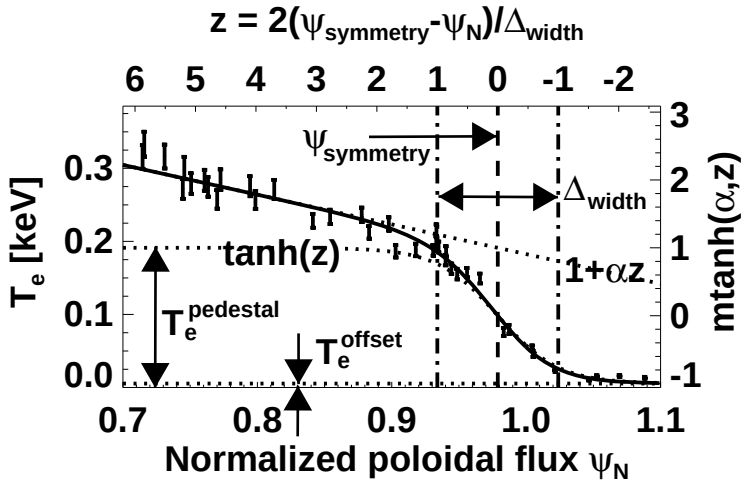

Figure 4: The mtanh fit captures the important elements of the H-mode pedestal with 5 intuitive parameters. An example electron temperature profile is shown. α_{slope} is the normalized slope inboard of the pedestal, with $\alpha_{slope} > 0$ indicating a monotonic profile and $\alpha_{slope} < 0$ indicating a hollow profile. T_e^{offset} is related to the temperature in the scrape-off layer, and $T_e^{pedestal}$ is approximately the temperature at the top of the pedestal. $\psi_{symmetry}$ and Δ_{width} are respectively the location and full width of the pedestal, or alternatively, the edge transport barrier.

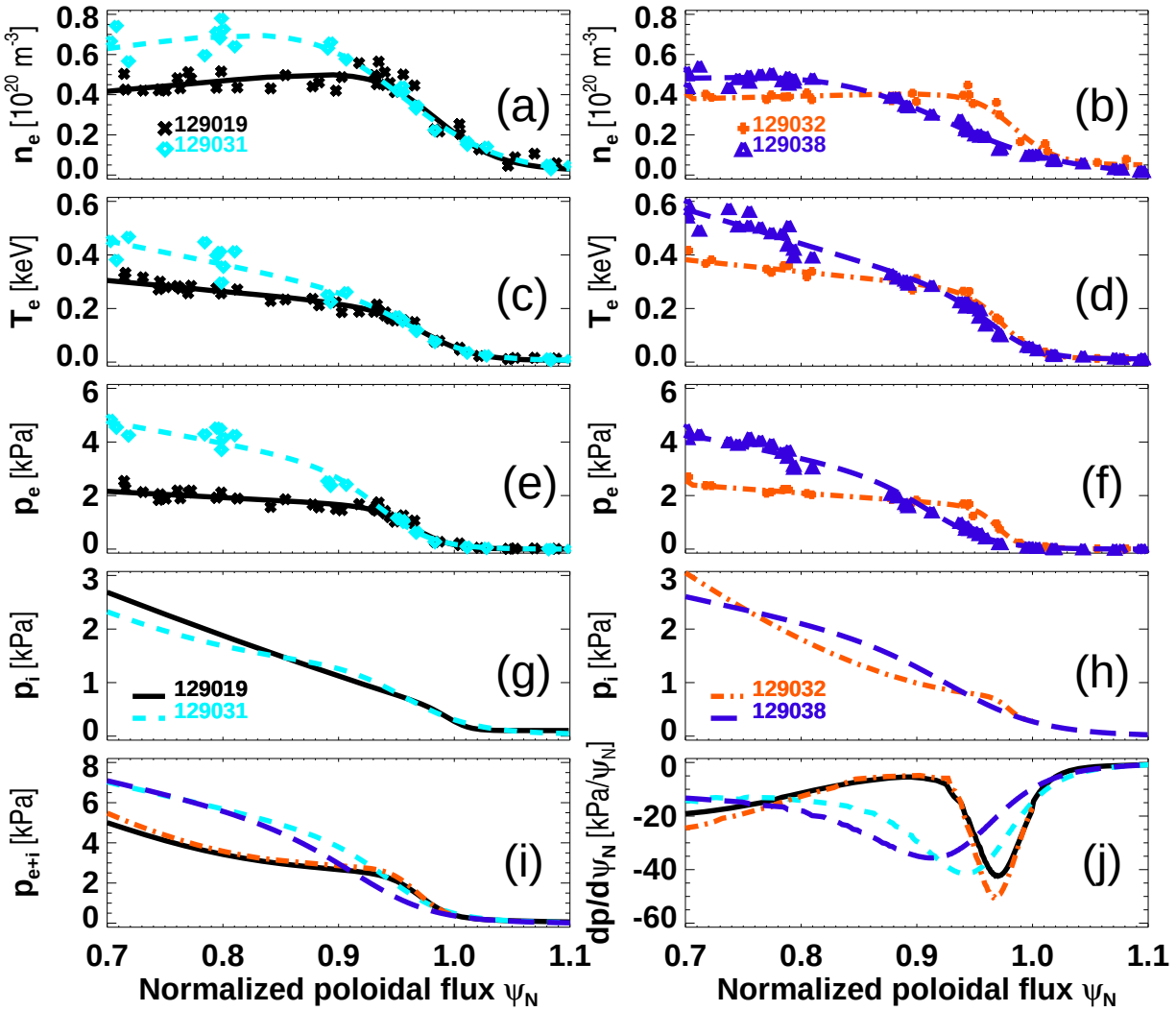

Figure 5: Lithium wall coatings drastically modified edge profiles. Edge profile comparisons of (a, b) electron density n_e, (c, d) electron temperature T_e, (e, f) electron pressure p_e, (g, h) ion pressure p_i, (i) total pressure p_{e+I}, and (j) pressure gradient $dp/d\psi_N$. Profiles are from a pre-lithium ELMy discharge (black X), an intermediate lithium discharge with reduced ELM activity (turquoise ◊), an intermediate lithium discharge where ELMs have returned (orange +), and a high lithium deposition, ELM-free discharge (blue Δ). Fits are obtained from multiple time slices mapped to the nearest equilibrium. The x-axis is normalized poloidal flux: $\psi_N = (\psi-\psi_{core})/(\psi_{separatrix}-\psi_{core})$, where ψ_{core} and $\psi_{separatrix}$ are the poloidal flux values at the magnetic axis and separatrix, respectively.

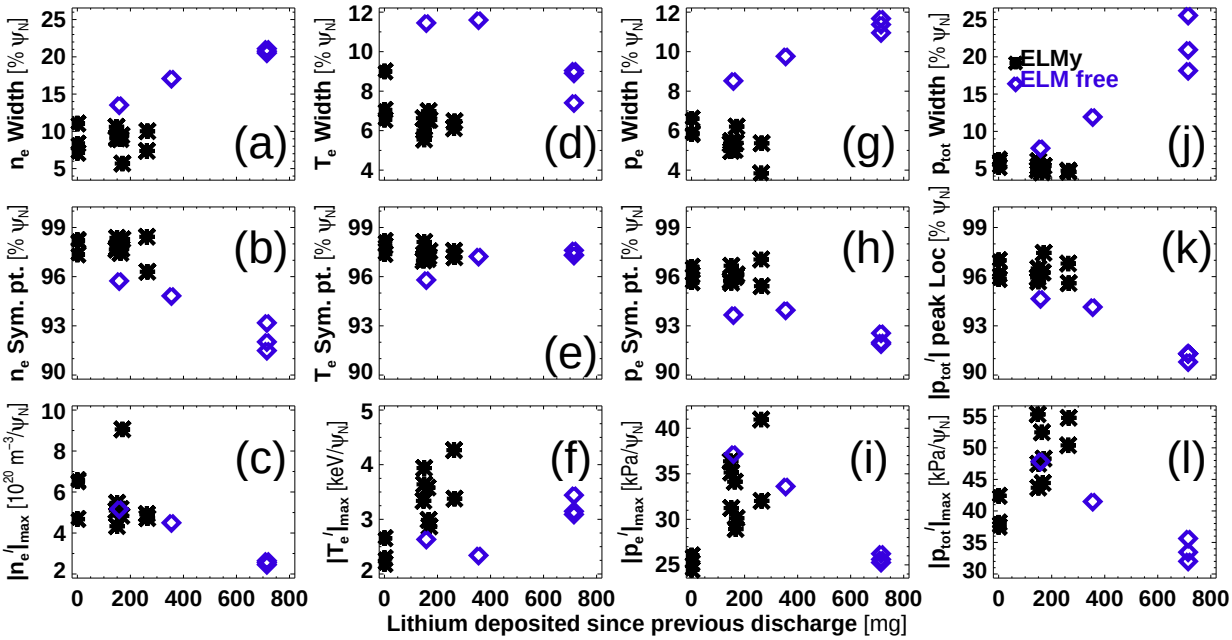

Figure 6: Density and pressure pedestals became wider and farther from separatrix with increasing lithium wall coatings while temperature showed no relationship to lithium. Lithium deposited since previous disharge is plotted vs. for ELMy (black *) and ELM free plasmas (blue ◊): (a) n_e mtanh full width, (b) n_e mtanh symmetry point, (c) peak n_e gradient, (d) T_e mtanh full width, (e) T_e mtanh symmetry point, (f) peak T_e gradient, (g) p_e mtanh full width, (h) p_e mtanh symmetry point, (i) peak p_e gradient, (j) p_{tot} full width at half maximum, (k) p_{tot} peak gradient location, and (i) peak p_{tot} gradient. Note that the vertical axes have suppressed zeros, and that the p_{tot} profile fit parameters are based on spline fits rather than mtanh fits.

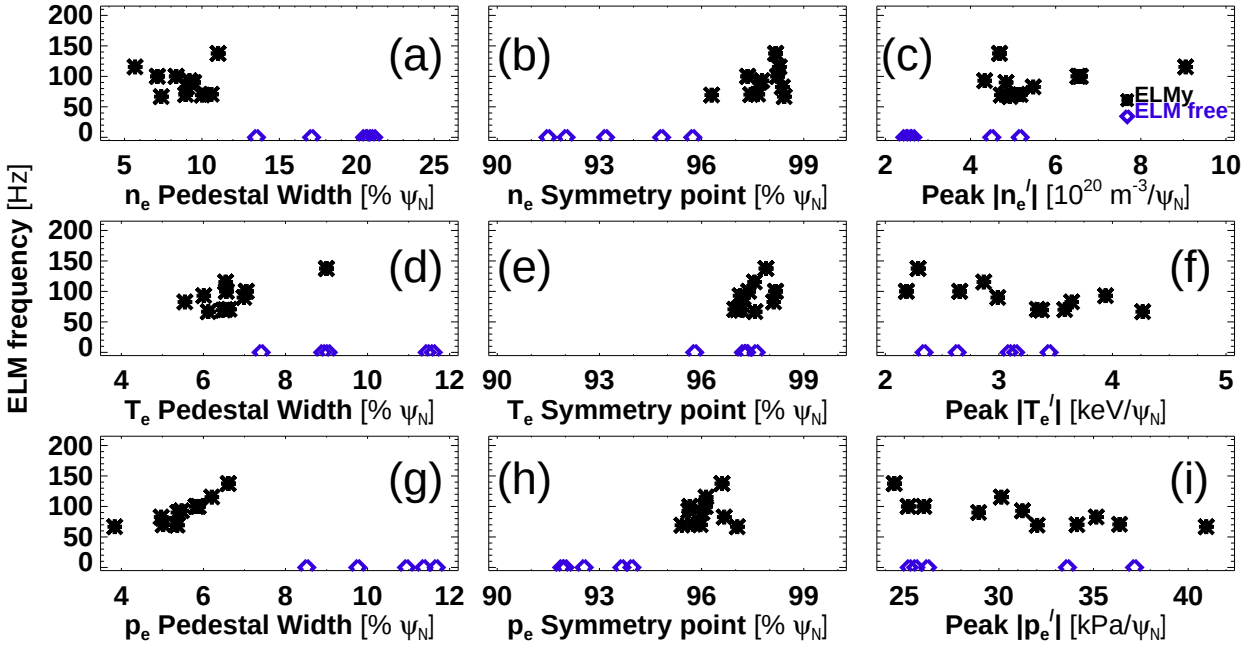

Figure 7: ELM free plasmas had wider density and pressure pedestals that are farther from the separatrix while pedestal gradients and temperature profiles showed no relationship to ELMs. ELM frequency is plotted vs. profile fit parameters for ELMy (black *) and ELM free plasmas (blue ◊): (a) n_e mtanh full width, (b) n_e mtanh symmetry point, (c) peak n_e gradient, (d) T_e mtanh full width, (e) T_e mtanh symmetry point, (f) peak T_e gradient, (g) p_e mtanh full width, (h) p_e mtanh symmetry point, and (i) peak p_e gradient. Note that the horizontal axes have suppressed zeros.

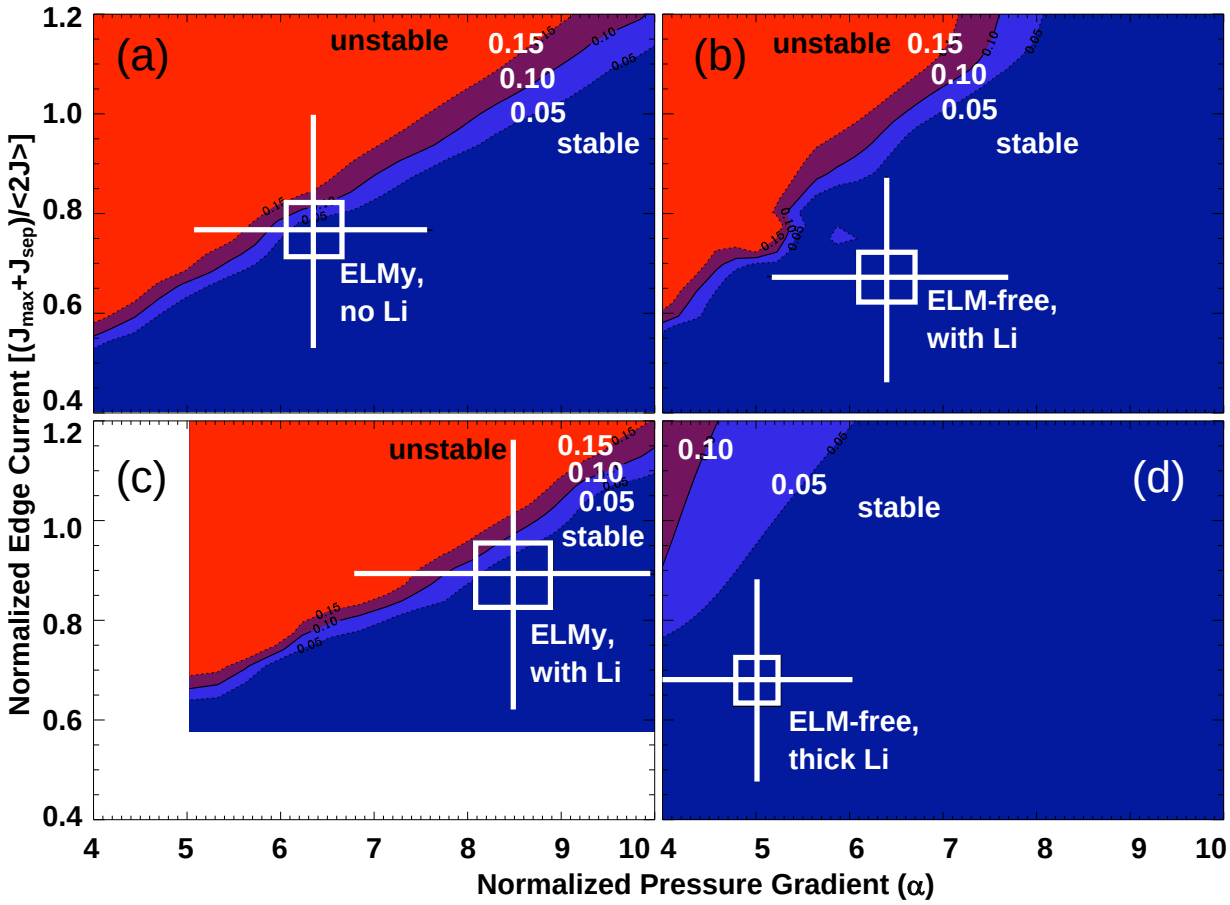

Figure 8: ELM-free plasmas were farther from the kink/peeling stability boundary as calculated by ELITE. Contour plots of the stability criterion, $\gamma_0/(½\ \omega_{*i})$ versus normalized edge current and normalized pressure gradient are shown for four representative discharges. The crosshairs are centered on the experimental equilibrium and represent relative error in normalized edge current and normalized pressure gradient of 30% and 20%, respectively. In the red region, $\gamma_0/(½\ \omega_{*i}) > 0.15$; in the blue region, $\gamma_0/(½\ \omega_{*i}) < 0.05$. Equilibria are from (a) a pre-lithium ELMy discharge, (b) an intermediate lithium discharge with reduced ELM activity , (c) an intermediate lithium discharge where ELMs have returned (no converged kinetic fits in blank space), and (d) a high lithium deposition, ELM-free discharge. Note that the axes have suppressed zeros.

References

[1] Federici G, Andrew P, Barabaschi P, *et al.* 2003 J. Nuc. Mat. **313-316**, 11-22

[2] Loarte A, Sugihara M, Kukushkin M, *et al*. 2008 *Proc. 22nd Fusion Energy Conf.* (*Geneva*) IT/P6-13.

[3] Zohm H 1996 Plasma Phys. and Control. Fusion **38**, 105-128.

[4] Loarte A, Saibene G, Sartori R, *et al.* 2003 Plasma Phys. Control. Fusion **45**, 1549-1569

[5] Oyama N, Gohil P, Horton L D, *et al.* 2006 Plasma Phys. Control. Fusion **48**, A171-A181

[6] Maingi R, Tritz K, Fredrickson E D, *et al.* 2005 Nucl. Fusion **45**, 264-270

[7] Connor J W, Hastie R J, and Taylor J B 1978 Phys. Rev. Lett. **40**, 396-399

[8] Manickam J 1992 Phys. Fluids B **4**, 1901

[9] Connor J W, Hastie R J, Wilson, H R, and Miller R L 1998 Phys. Plasmas **5**, 2687

[10] Lang P T, Kallenbach A, Bucalossi J, *et al.* 2005 Nucl. Fusion **45**, 502-511

[11] Canik J M, Maingi R, Evans T E, *et al.* 2010 Phys. Rev. Lett. **104**, 1-4

[12] Canik J M, Sontag AC, Maingi R, *et al.* 2010 Nucl. Fusion **50**, 064016

[13] Greenfield C M, Burrell K H, DeBoo J C, *et al.* 2001 Phys. Rev. Lett. **86**, 4544-4547

[14] Evans T, Moyer R, Thomas P, *et al.* 2004 Phys. Rev. Lett. **92**, 9-12

[15] Osborne T H, Snyder P B, Burrell K H, *et al.* 2008 J. Phys.: Conf. Series **123**, 012014

[16] Krasheninnikov S I, Zakharov L E, and Pereverzev G V 2003 Phys. Plasmas **10**, 1678

[17] Zakharov L, Blanchard W, Kaita R, *et al.* 2007 J. Nuc. Mat. **363-365**, 453-457

[18] Mansfield D K, Hill K W, Strachan J D, *et al.* 1996 Phys. Plasmas **3**, 1892

[19] Majeski R, Doerner R, Gray T, *et al.* 2006 Phys. Rev. Lett. **97**, 1-4

[20] Majeski R, Berzak L, Gray T, *et al.* 2009 Nucl. Fusion **49**, 055014

[21] Ono M, Kaye S M, Peng Y-K M, *et al.* 2000 Nucl. Fusion **40**, 557-561

[22] Kugel H W, Bell M G, Bell R, *et al.* 2007 J. Nuc. Mat. **363-365**, 791-796

[23] Kugel H W, Bell M G, Ahn J-W, *et al.* 2008 Phys. Plasmas **15**, 056118

[24] Kugel H W, Mansfield D, Maingi R, *et al.* 2009 J. Nuc. Mat. **390-391**, 1000-1004

[25] Mansfield D K, Kugel H W, Maingi R, *et al.* 2009 J. Nuc. Mat. **390-391**, 764-767

[26] Maingi R, Osborne T H, LeBlanc B P, *et al.* 2009 Phys. Rev. Lett. **103**, 18-21

[27] Canik J M, Maingi R, Kubota S, *et al.* 2011 Phys. Plasmas **18** 056118

[28] Maingi R, Boyle D, Canik J M, *et al.* 2010 *Proc. 23rd Fusion Energy Conf.* (*Daejon, Korea*) EX/D2-2.

[29] Maingi R, Hubbard A E, Meyer H, *et al.* 2011 Nucl. Fusion **51** 063036

[30] Kugel H W, Bell M G, Schneider H, *et al.* 2010 Fusion Engineering and Design **85**, 865-873

[31] Bell M G, Kugel H W, Kaita R, *et al.* 2009 Plasma Phys. Control. Fusion **51**, 124054

[32] Maingi R, Kaye S M, Skinner C H, *et al.* 2011 Phys. Rev. Lett. (at press)

[33] LeBlanc B P, Bell R E, Johnson D W, *et al.* 2003 Revi. Of Sci. Instruments **74**, 1659

[34] Bell R E, Andre R, Kaye S M, *et al.* 2010 Phys. Plasmas **17**, 082507

[35] Lao L L, St. John H, Stambaugh R D, *et al.* 1985 Nucl. Fusion **25**, 1611-1622

[36] Sabbagh S A, Kaye S M, Menard J, *et al.* 2001 Nucl. Fusion **41**, 1601-1611

[37] Groebner R J, Baker D R, Burrell K H, *et al.* 2001 Nucl. Fusion **41**, 1789-1802

[38] Groebner R J and Osborne T H 1998 Phys. Plasmas **5**, 1800

[39] Sauter O, Angioni C, and Lin-Liu Y R 1999 Phys. Plasmas **6**, 2834-2839

[40] Thomas D, Leonard A, Lao L, *et al.* 2004 Phys. Rev. Lett. **93**, 1-4

[41] Wilson H R, Snyder P B, Huysmans G T A, and Miller R L 2002 Phys. Plasmas **9**, 1277
[42] Snyder P B, Wilson H R, Ferron J R, *et al.* 2002 Phys. Plasmas **9**, 2037
[43] Sontag A C, Canik J M, Maingi R, *et al.* Nuclear Fusion (at press)

The Princeton Plasma Physics Laboratory is operated
by Princeton University under contract
with the U.S. Department of Energy.

Information Services
Princeton Plasma Physics Laboratory
P.O. Box 451
Princeton, NJ 08543

Phone: 609-243-2245
Fax: 609-243-2751
e-mail: pppl_info@pppl.gov
Internet Address: http://www.pppl.gov